https://dx.doi.org/10.21577/0103-5053.20220148

J. Braz. Chem. Soc., Vol. 34, No. 6, 794-808, 2023

Article

Facile Methods for the Assembly of Large-Area Perovskite Solar Cells and Mini-Module: A Step-by-Step Description of Layers Processing

Francineide L. de Araújo,[a,b] *Ana F. Nogueira*[*,a] *and Jilian N. de Freitas*[*,b]

[a]*Laboratório de Nanotecnologia e Energia Solar (LNES), Instituto de Química, Universidade Estadual de Campinas (UNICAMP), 13083-970 Campinas-SP, Brazil*

[b]*Centro de Tecnologia da Informação Renato Archer (CTI), Rodovia D. Pedro I, km 143.6, 13069-901 Campinas-SP, Brazil*

Hybrid organic-inorganic perovskites have attracted interest in photovoltaic applications due to their excellent optoelectronic properties and low-temperature processability. From 2009 to 2021, lab-scale perovskite solar cells (PSC) reached a power conversion efficiency (PCE) of 25.7%, and a PCE of 17.9% for perovskite solar modules with an area of 800 cm^2. Here, we present an investigation using three deposition techniques, spin-coating, blade-coating, and spray-coating, to process the charge transport layers and the active layer of perovskite solar cells onto 5 cm × 5 cm sized substrates, with device structure glass/fluorine-doped tin oxide (FTO)/c-TiO_2/meso-TiO_2+Perovskite/2,2',7,7'-tetrakis(*N*,*N*-di-*p*-methoxyphenyl-amine)9,9'-spirobifluorene (spiro-OMeTAD) or poly(3-hexylthiophene) (P3HT)/Au. Large-area PSC achieved an open-circuit voltage of around 1.1 V and PCE of 6%. The power generated was sufficient to start a fan. Furthermore, the connection in series of two large-area PSCs generated a voltage of 1.9 V. Then, we developed a simple method for manufacturing a monolithic perovskite mini-module containing two series-connected PSCs without using laser-scribing processes (usually named P1, P2, and P3 processes). This mini-module delivered a voltage of 1.52 V. Both voltages (1.9 and 1.52 V) were enough to turn on a red (or yellow) light-emitting diode (LED). To our knowledge, this is the first scientific report describing the assembly of a large-area n-i-p perovskite single cell and mini-module in Brazil.

Keywords: perovskite solar cells, large area, mini-module, deposition methods

Introduction

Hybrid organic-inorganic perovskites with the general formula ABX_3 (A = organic cation, B = inorganic cation, and X = halide anion) are semiconductor materials that can be used in various optoelectronic devices, such as perovskite solar cells (PSCs).[1-8] These materials are promising for application in photovoltaics due to their extraordinary optical and electronic properties, such as high charge mobility and absorption coefficient, low excitation binding energy, long diffusion length, and low-temperature processability.[9-15] In just a few years (from 2009 to 2021), lab-scale (active area of ca. 0.1 cm^2) PSCs fabricated by spin-coating methods have reached a power conversion efficiency (PCE) of 25.7%. In contrast, a PCE of 23.2% was achieved for PSCs processed by blade-coating (scalable technique).[16-18] On the other hand, a perovskite solar module (PSM) with an area of 19.32 cm^2 achieved a reported PCE of 21.4%, and a PCE of 17.9% for a module with 804 cm^2, as reported in the Solar Cell Efficiency Tables (version 59).[17,19] Although the efficiency of PSMs has increased over the years,[19] reaching relatively high values, they are still quite behind the efficiencies achieved in lab-scale PSCs, so scaling up this technology remains a challenge for commercial progress.[20-22] The difference between PCE values in small or large-area cells is related to the quality of the layers deposited over large substrates, mainly that of the perovskite layer, resulting in defects, pinholes, incomplete coverage, low crystallinity and poor morphology, for instance.[23-25]

The fabrication techniques employed for the assembly of highly-efficient lab-scale PSCs are usually not scalable (spin-coating, for example). Thus, much of the knowledge generated in those researches cannot be directly transferred to the fabrication of large-area PSCs.[26] The use of unsuitable techniques for manufacturing large-scale devices would result

*e-mail: anafla@unicamp.br; jilian.freitas@cti.gov.br
Editor handled this article: Rodrigo A. A. Muñoz (Associate)

in low efficiency, waste of materials, poor reproducibility and a high production cost. Additionally, the small-area PSCs are usually assembled under controlled ambient, i.e., under an inert atmosphere inside a glove box. When considering the upscaling of PSCs, easiness of preparation, low cost, and use of accessible materials with low toxicity, and processes and techniques compatibility with a roll-to-roll production line in air (without using a controlled, inert atmosphere) should be pursued. Table S1 (Supplementary Information (SI) section) summarizes the current state-of-the-art of large-area PSCs/PSMs reported in the international scientific literature. The main results published by different research groups in the last four years are displayed in terms of the device structure, PCE, module size, and a summary of the main novelty achieved in those works. The references were organized considering the highest PCE value reached in each work.

One of the key points to increase the photovoltaic performance of large-area PSCs/PSMs is the use of different deposition methods and processing conditions to obtain more homogeneous films on large substrates and, consequently, an optimized morphology. In recent years, different deposition techniques have been investigated to assemble large-area perovskite solar cells. Those methods include common lab-scale techniques, such as spin-coating, and techniques that could be scalable to semi-industrial or industrial processes, such as spray-coating, screen printing, inkjet printing, slot-die coating, and blade-coating.[27-30]

In this work, we present an investigation of three techniques, spin-coating (Figure 1a), blade-coating (Figure 1b), and spray-coating (Figure 1c), for the processing of the charge transport layers (electron transport layer (ETL) and hole transport layer (HTL)) and the active layer of perovskite solar cells using 5 cm × 5 cm sized substrates as basis. Figure 1d illustrates the structure of the devices (glass/FTO/ETL/Perovskite/HTL/Au), and Figure 1e shows the energy levels of the components. The first step focused on the optimization of the layers of large-area PSCs: patterned transparent conductive electrode (FTO), electrons transport layer (ETL = c-TiO_2/Meso-TiO_2), active layer ($MAPbI_3$ or CsFAMA), and hole transport layer (HTL = P3HT or spiro-OMeTAD). Then, the assembly of a complete large-area PSC (9 cm^2 active area) was demonstrated using the better experimental conditions found in the previous step. In addition, a simple method of manufacturing a monolithic perovskite solar module (5 cm × 5 cm size substrate) with two series-connected perovskite solar cells without the use of lasers (P1, P2, and P3 scribing processes commonly used)[31-33] was demonstrated. The large-area PSC and PSM were used to spin a fan and to turn on a red (or yellow) light-emitting diode (LED).

Experimental

Materials

Methylammonium iodide (MAI), methylammonium bromide (MABr), formamidinium iodide (FAI), tris(2-(1*H*-pyrazol-1-yl)-4-*tert*-butylpyridine)cobalt(III)

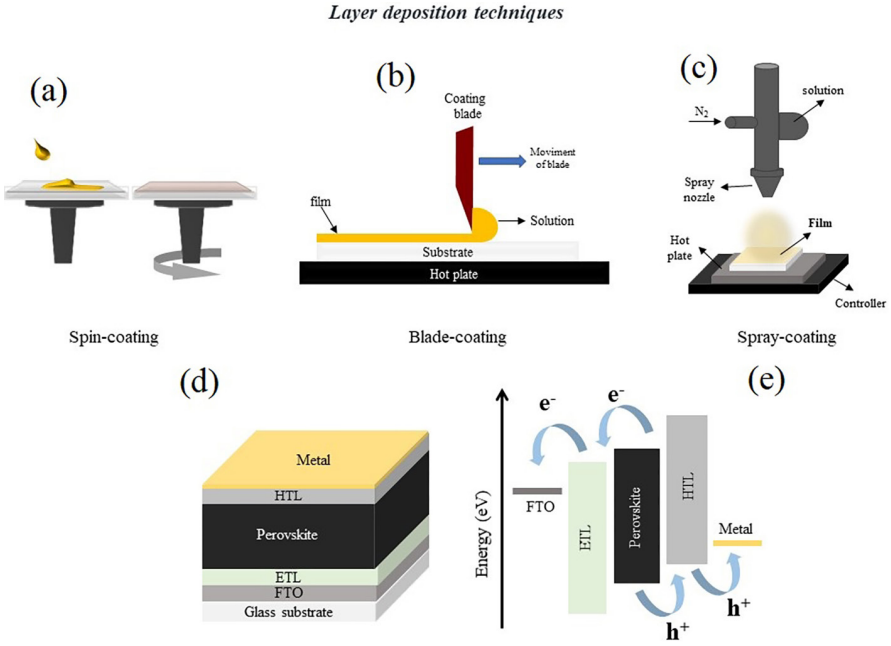

Figure 1. Methods used in the deposition of the layers of the PSCs: (a) spin-coating, (b) blade-coating, and (c) spray-coating. (d) Structure of conventional mesoscopic n-i-p device configuration used in this work. (e) Schematic energy levels diagram of the perovskite solar cell, showing the processes of the separation and collection of charges (electrons e^- and holes h^+).

tri[bis(trifluoromethane)sulfonimide] (FK209 Co^{III} TFSI), and fluorine-doped tin oxide (FTO)-coated glasses substrates (TEC7-300 mm × 300 mm × 2.2 mm) were acquired from GreatCell Solar Materials LTD (Queanbeyan, Australia). Lead iodide (PbI_2, 99.99%), cesium iodide (CsI, 99.9%) and lead bromide ($PbBr_2$, > 98%) were acquired from Tokyo Chemical Industry (TCI) Co., Ltd. (Oxford, United Kingdom). Anhydrous solvents (dimethyl formamide (DMF), dimethyl sulfoxide (DMSO), 2-methoxyethanol (2-ME), *N*-methyl-2-pyrrolidone (NMP), acetonitrile (CAN), chlorobenzene (CB), terpineol, isopropanol and ethanol (EtOH)), 4-*terc*-butyl pyridine (tBP, 98%), lithium bis(trifluoromethanesulfonyl)imide (LiTFSI; 99.95%), tin(IV) chloride pentahydrate ($SnCl_4.5H_2O$), lead(II) acetate trihydrate ($Pb(CH_3CO_2)_2{\cdot}3H_2O$), and lead(II) chloride ($PbCl_2$) were purchased from Sigma-Aldrich (Barueri, São Paulo). Poly(3-hexylthiophene) (P3HT; molar weight 70,000 kDa, regioregular) was acquired from 1-material Inc. (Quebec, Canada). 2,2',7,7'-Tetrakis(*N*,*N*-di-*p*-methoxyphenyl-amine)9,9'-spirobifluorene (spiro-OMeTAD) was purchased from Xi'an Polymer Light Technology Corp (Shaanxi, China).

Precursor solutions preparation

Two precursor solutions were used for the ETL: for the compact TiO_2 layer were used 0.4 mL of acetylacetone and 0.6 mL of titanium diisopropoxide bis(acetylacetonate) in 9 mL of ethanol (this solution was used for spray deposition); for mesoporous-TiO_2 (concentration of 150 mg mL^{-1}) were used 750 mg of Dyesol paste (30 NR-D) in 5 mL of ethanol (deposited by blade-coating or spin-coating). Table 1 shows the compositions of the perovskite precursor solutions prepared for the deposition of the perovskite films. All the solutions were stirred at room temperature for 12 h to achieve complete dissolution of the precursors. The methylammonium lead triiodide ($MAPbI_3$) solutions were prepared in air, and the cesium formamidinium methylammonium (CsFAMA) solution was prepared in controlled ambient (glovebox with N_2) according to the procedure described by Saliba *et al.*[34]

Substrate preparation

FTO glass substrates (5 cm × 5 cm) were used as the transparent conductive layer. FTO substrates were patterned using zinc powder and hydrochloric acid (4 M) for chemical etching, and an etch-resistant tape (Kapton) was used to protect the part which would not be corroded. Figures S1 and S2 (SI section) show the steps to standardize the FTO glass substrate for assembling large-area PSCs and mini-PSMs with two cells connected in series without the use of laser-scribing processes, respectively. Patterned FTO-glass substrates were cleaned in an ultrasonic bath with Hellmanex 2% solution for 25 min, followed by distilled water and isopropyl alcohol for 10 min each, dried under nitrogen gas flow, and treated in a UV-ozone chamber for 25 min.

Optoelectronic characterization

UV-Visible absorption spectroscopy

UV-Vis absorption spectra of the perovskite films were acquired using an Agilent spectrophotometer (Santa Clara, United States), model Cary 60, in the 200-1000 nm range. Transmission spectra of ETL were obtained using the same equipment in T% mode.

Field emission scanning electron microscopy (FEG-SEM)

FEG-SEM images were obtained using a Quanta 250 microscope from FEI Company (Hillsboro, United States) coupled with a field emission-scanning (FEG-SEM) and were collected to investigate surface morphologies of the samples (homogeneity and grain perovskite size).

Atomic force microscopy (AFM)

Images of the perovskite films were obtained in a Easyscan 2 FlexAFM from Nanosurf (Liestal, Switzerland) using a NSC14/Cr-Au tip in the tapping mode.

Table 1. Preparation of perovskite precursor solutions

Perovskite solution	Composition	Solvent	Final concentration of the solution / M
$MAPbI_3$	PbI_2 and MAI	DMF:DMSO (4:1 v/v)	1.2
$MAPbI_3$	$PbCl_2$, $Pb(Ac)_2$, and MAI	2-ME	0.5
$MAPbI_3$	$PbCl_2$, $Pb(Ac)_2$, and MAI	DMF	1.0
CsFAMA ($Cs_{0.05}FA_{0.85}MA_{0.10}Pb(I_{0.83}Br_{0.17})_3$)	PbI_2, $PbBr_2$, MABr, CsI and FAI	DMF:DMSO (4:1 v/v)	1.5

MAI: methylammonium iodide; MABr: methylammonium bromide; FAI: formamidinium iodide; $PbAc_2$: lead acetate(II); $PbCl_2$: lead chloride(II); PbI_2: lead iodide(II); DMF: dimethyl formamide; DMSO: dimethyl sulfoxide; 2-ME: 2-methoxyethanol; CsI: cesium iodide; $PbBr_2$: lead bromide.

Perfolometry

Film thickness was measured using a mechanical Dektak XT profilometer (Bruker, Massachusetts, United States).

Current-voltage (J-V) curves

J-V curves under illumination (100 mW cm^{-2}) were measured using a solar simulator (Air Mass 1.5G filter, HAL-320, Asahi Spectra Co., Ltd., Torrance, United States). The light intensity was calibrated using a reference silicon solar cell with a KG5 filter (PV Measurements, Inc.). A Keithley 2400 SourceMeter (Cleveland, United States) was used for the J-V measurements in a voltage range from 0 to 1.2 V (forward scan) and +1.2 to 0 V (reverse scan) with steps of 10 mV and a delay time of 0.25 s.

Results and Discussion

Optimization of the layers

One of the biggest challenges in manufacturing large-area solar cells is the efficient application of thin film deposition methods onto large substrates. The quality of each layer that constitutes the photovoltaic device is paramount to reaching good device performance. Herein, different scalable deposition techniques were investigated for the deposition of the PSC layers onto substrates with dimensions of 5 cm × 5 cm. These methods included the standard lab-scale method, spin-coating, and spray-coating and blade-coating techniques, which could be scalable to semi-industrial or industrial processes. Table 2 lists the methods used for the deposition of each layer. Herein, we will discuss our efforts to optimize each layer during the assembly of PSCs in 5 cm × 5 cm substrates.

Transparent conductive layer

FTO-glass substrates were used as the transparent conductive contact. The transmittance of these substrates is an essential factor for the efficient passage of light.[35] Thus, before manufacturing the large-area devices, a brief evaluation of the uniformity of the transmittance within a total area of 5 cm × 5 cm of the FTO-glass substrates purchased from GreatCell was realized. Figure 2a shows a photo of an FTO substrate divided in four regions, and Figure 2b shows the transmission spectra obtained from each area. It was observed that at 600 nm, the transmission is about 75%, and the variation between the regions is less than 2%, which was considered adequate for use in devices with sizes up to 5 cm × 5 cm. AFM topography image (5 μm × 5 μm scan size) with the value of root-mean-square (RMS) surface roughness and top-view SEM image showing the surface morphology of the same FTO substrate are shown in Figures 2c and 2d, respectively.

Table 2. Methods investigated in this work for the deposition of the layers of PSCs

Layer	Deposition method
c-TiO_2	spray-coating
meso-TiO_2	spin-coating or blade-coating
CsFAMA	spin-coating
$MAPbI_3$	spin-coating or blade-coating
Spiro-OMeTAD	spin-coating
P3HT	spin-coating or blade-coating

c-TiO_2: compact titanium oxide; meso-TiO_2: mesoporous TiO_2; MA: methylammonium; FA: formamidinium; Cs: cesium; $MAPbI_3$: methylammonium lead iodide; Spiro-OMeTAD: 2,2',7,7'tetrakis-(*N*,*N*-di-4-methoxyphenylamino)-9,9'-spirobi-fluorenes; P3HT: poly(3-hexylthiophene).

Electron transport layer (TiO_2)

Subsequently to the preparation of the FTO-glass substrate, the first cell component to be optimized was the ETL consisting of two layers: compact-TiO_2 (c-TiO_2) and mesoporous TiO_2 (meso-TiO_2). Overall, the spray-coating method (Figure 1c) has been considered a promising scalable technique for the deposition of compact layers with thicknesses of about 20-30 nm, due to the low cost and waste of material of that technique.[34,36,37] In this step, we used only the spray-coating method for the deposition of a compact-TiO_2 layer onto FTO-glass substrates, following a protocol developed by Saliba *et al.*[34] for small cells (6 mm^2). For that, we used a standard paint gun (Figure 3a) with a compartment for solution storage. In ambient conditions, the c-TiO_2 solution (Figure 3c) was deposited in a total area of 10 cm × 10 cm (corresponding to a total of four FTO substrates of 5 cm × 5 cm each), according to Figure 3b. A part of the FTO (about 0.5 cm) was protected with adhesive tape.

The amount of 10 mL of c-TiO_2 solution (Figure 3c) was tested since the deposition system (gun) used here was different from the spray-coating system used in the reference.[34] Before deposition, the gun was adjusted to ensure an aerosol flow. Moreover, before deposition of the c-TiO_2 precursor solution, the substrates were preheated to approximately 450 °C in a hot plate (with uniform temperature distribution, Figure 3b) for 10 min and kept at this temperature throughout the spray deposition. Figure 3d shows a bare FTO substrate and c-TiO_2 film on the FTO substrate obtained in this condition by spray-coating, showing a uniform film. The amount of 10 mL of solution using the ordinary paint gun was enough to deposit an electron blocking layer[38,39] in a total area of 10 cm × 10 cm

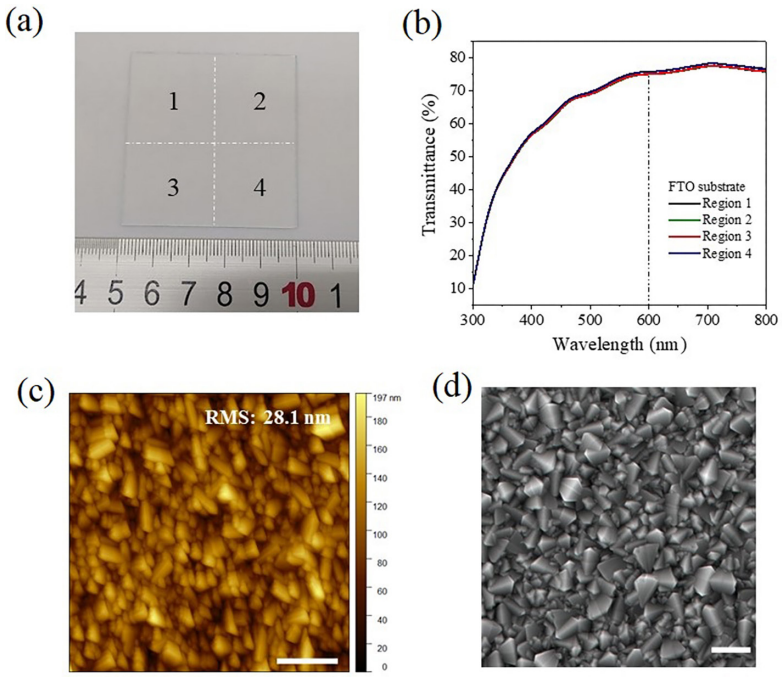

Figure 2. (a) Photo of the FTO-glass substrate (5 cm × 5 cm size). (b) Transmission spectra of FTO substrate, collected in the four regions depicted in (a). (c) AFM topography image (5 μm × 5 μm scan area) and (d) FEG-SEM image showing the surface morphology of the FTO-glass substrate used in this work. The scale bar represents 1 μm in both images.

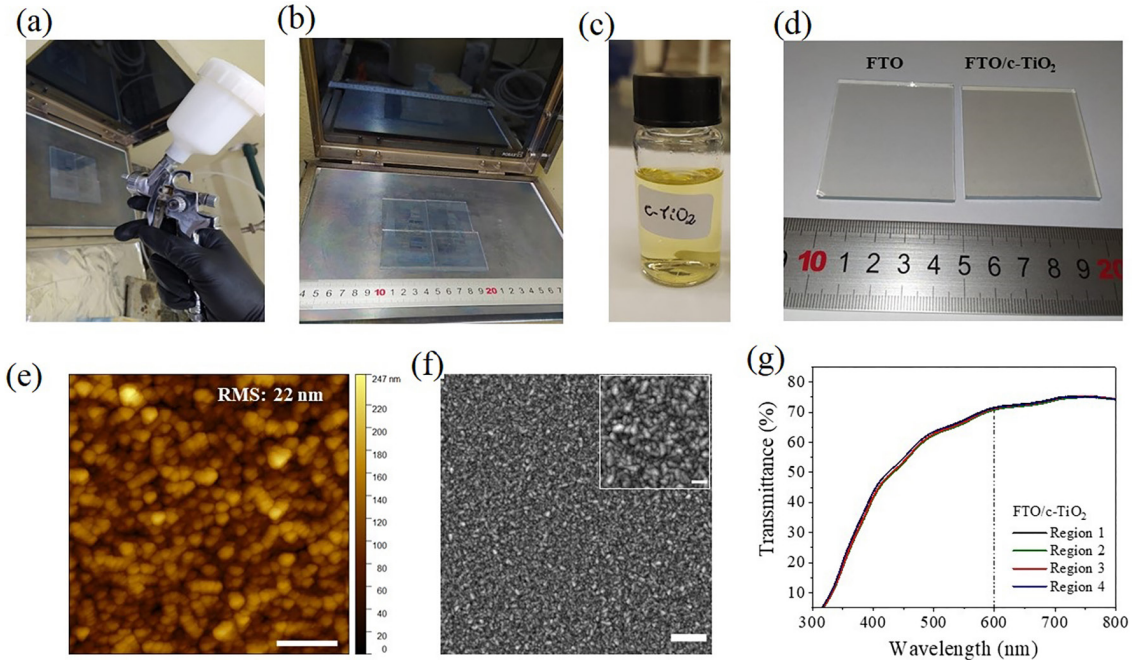

Figure 3. (a) Spray-coating setup and (b) four FTO substrates (size of 5 cm × 5 cm each) over a hot plate (after deposition at 450 °C). (c) Photo of c-TiO_2 precursor solution (0.4 mL of acetylacetone and 0.4 mL of titanium diisopropoxide bis(acetylacetonate) in 9 mL of ethanol (10 mL total). (d) Photo of bare FTO substrate and FTO/c-TiO_2 film deposited by spray-coating. (e) AFM topography image (5 μm × 5 μm scan area) and (f) FEG-SEM image showing the surface morphology of the c-TiO_2 layer. The scale bar represents 1 μm in both images.

(4 substrates of 5 cm × 5 cm each), as verified with cyclic voltammetry measurements (Figure S3, SI section). AFM (Figure 3e) and SEM (Figure 3f) images were collected to investigate the surface morphology of the sprayed c-TiO_2 film. As shown in Figure 3e, the glass FTO substrate was completely covered with the c-TiO_2 layer, and the RMS surface roughness was 22 nm. The thickness measured was 32 nm, a value considered adequate for this layer, according to references.[34,40] SEM image (Figure 3f) also shows that the c-TiO_2 layer is homogeneous, has good coverage and

uniformity, and is free of pinholes. The transmittance spectra acquired in 4 different regions of the c-TiO_2 film are shown in Figure 3g. At a wavelength of 600 nm, the transmittance was 71%, with a small reduction in relation to the transmittance of the bare FTO substrate (Figure 2a).

The subsequent layer, mesoporous TiO_2, provides a structure to assist infiltration of the perovskite absorber material and selectively extract electrons from the perovskite layer, as well as act as a blocking layer to increase the performance of PSCs.[41] After formation of the c-TiO_2 layer, the meso-TiO_2 layer was prepared. Before the deposition of the TiO_2 paste, a surface treatment of c-TiO_2 films was performed by UV-ozone for 15 min. This step is crucial for better spreading the mesoporous layer over the c-TiO_2 layer.

The meso-TiO_2 films were then deposited either by spin-coating or by blade-coating. We chose a condition for the spin-coating deposition based on a previous work for lab-scale PSCs.[42] Two conditions, with different TiO_2 paste concentrations (150 and 75 mg mL^{-1}), were investigated for deposition by blade-coating at room temperature. Thereafter, the films were sintered in multiple temperatures steps (maximum of 450 °C), as reported by Saliba *et al*.[34] Table 3 summarizes the parameters used in each deposition method: the amount of paste necessary to cover the entire substrate, the spinning rotation or gap between blade/substrate, and the thickness of the films. It should be noted that the amount of solution (Figure 4a) required to form the meso-TiO_2 film on substrates with a size of 5 cm × 5 cm via spin-coating (600 µL) was about 7.5 times higher than the amount used in the blade-coating method (80 µL). The same happens for the other layers (perovskite, P3HT and spiro-OMeTAD layers), as will be discussed later. This is one of the main advantages of the use of the blade-coating method, where solution waste becomes minimal.

Figures 4b-4d shows the photographs and AFM images with the RMS value of surface roughness of FTO/c-TiO_2/meso-TiO_2 layers deposited by spin-coating (paste concentration of 150 mg mL^{-1}), and by blade-coating (150 and 75 mg mL^{-1}). The films show thicknesses (and RMS) of 180 (23.2), 315 (29.0), and 132 nm (27.0 nm), respectively. According to the literature,[34] the ideal value for the meso-TiO_2 layer thickness is about 100-150 nm. Thus, we can consider that the conditions achieved by spin-coating or blade-coating (from a solution with a concentration of 75 mg mL^{-1} of TiO_2) can be used to obtain meso-TiO_2 films with appropriate thicknesses.

The glass/FTO/c-TiO_2/meso-TiO_2 samples were also analyzed by collecting the transmittance spectra, as shown in Figure 4e. At 600 nm, the FTO substrate has a transmittance of 75%, whereas the transmittance of spin-coated meso-TiO_2 was 80.2%, and blade-coated meso-TiO_2 layers were 79.3% for a solution with a concentration of 150 mg mL^{-1}, and 83% for a solution with a concentration of 75 mg mL^{-1}. According to the spectra, we can observe that the samples containing meso-TiO_2 films deposited onto FTO/c-TiO_2 substrates presented higher transmittance values than FTO/c-TiO_2 (Figure 3f). Other authors have also observed higher transmittance values after deposition of the meso-TiO_2 layer as well,[43] and this might arise from interference effects. Regardless of the cause, this can be understood as a positive effect, since higher transmittances indicate a higher passage of sunlight, which can easily pass through the FTO/c-TiO_2/meso-TiO_2 layers to be absorbed by the perovskite active layer.

Perovskite film (active layer)

The formation of high-quality perovskite films on large substrates has been considered one of the main challenges to manufacturing efficient, low-cost perovskite solar modules.[44] Herein, we investigated the deposition of the perovskite layers onto substrates of 5 cm × 5 cm, using as a starting point the deposition used in previous works of our group on small PSCs by spin-coating and blade-coating.[42,45-48] We observed that adjustments were necessary for the deposition over larger areas, so other compositions were also tested, as will be discussed in the next sections.

Large area perovskite films via spin-coating

For manufacturing good films over large substrates using the spin-coating deposition with the antisolvent approach, we performed some tests with different parameters than those used for small-scale PSCs (Figure S4, SI section). This step was very important since

Table 3. Deposition parameters and thickness of the meso-TiO_2 films

Deposition method	Concentration / (mg mL^{-1})	Solution volume / µL	Speed	Acceleration / (rpm s^{-1})	Thickness / nm
Spin-coating	150	600	4000 rpm/30 s	2000	180 ± 1.4
				Gap / µm	
Blade-coating	150	80	10 mm s^{-1}	50	315 ± 3.3
	75				132 ± 2.5

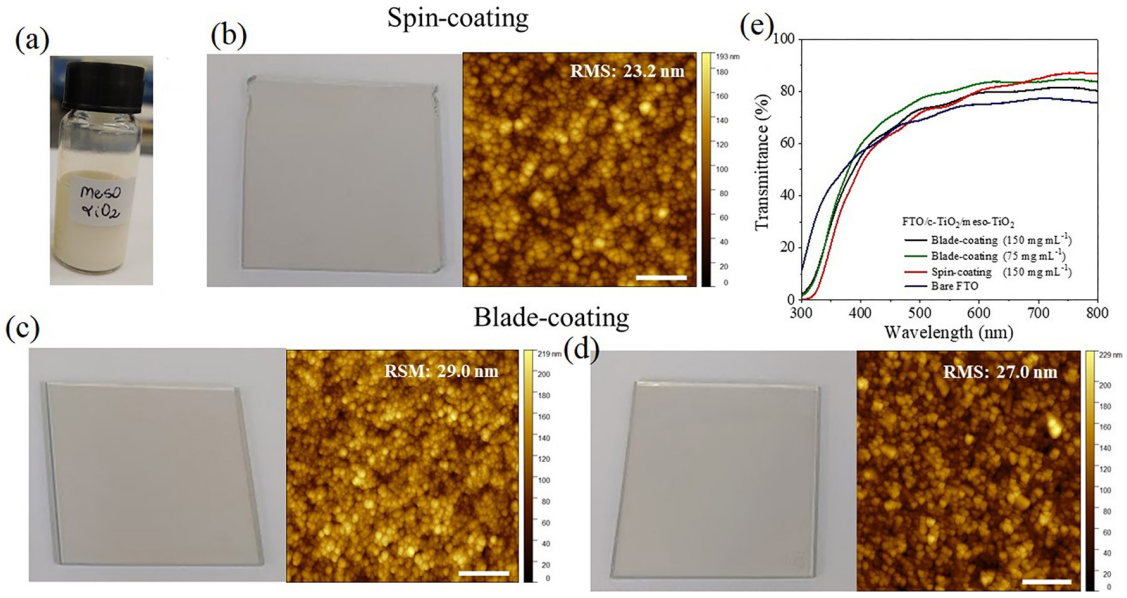

Figure 4. (a) Meso-TiO_2 precursor solution (5 mL of volume) prepared by diluting 750 mg of TiO_2 paste (30 NR-D, Dyesol) in 5 mL of ethanol. Photograph and AFM images (5 μm × 5 μm of scan area) with the respective RMS value of the FTO/c-TiO_2/meso-TiO_2 layers deposited by: (b) spin-coating, (c) blade-coating (150 mg mL^{-1}) or (d) blade-coating (75 mg mL^{-1}). (e) Transmittance spectra of the films. The scale bar represents 1 μm in all AFM images.

spin-coating is inadequate for depositing perovskite films over large substrates.[49] Nevertheless, it is interesting to note that several works reporting perovskite mini-modules still have used this method.[50-52]

Perovskite films were deposited inside a glove box. $MAPbI_3$ and CsFAMA solutions were prepared in a mixture of DMF:DMSO (4:1 v/v), as detailed in Table 3. The amount of solution required to cover the entire FTO substrate was 600 μL. Figures S4b-S4c shows $MAPbI_3$ films with defects generated during CB antisolvent drip. In this case, for the dripping of the antisolvent, a micropipette plastic tip of 1 mL (Figure S4a, left) filled with either 200 or 700 μL of CB was used. However, better results were obtained using a tip of 1 mL with a cut about 2 cm from the thinner edge (Figure S4a, right) and 700 μL of CB, to deposit both $MAPbI_3$ and CsFAMA perovskites, as shown in Figures S4d-S4e, respectively. Through this strategy, it was possible to drop the antisolvent over the perovskite film uniformly, resulting in a much more homogeneous film than the one obtained when using the regular tip (1 mL tip without cut). To our knowledge, this strategy of antisolvent deposition onto 5 cm × 5 cm substrates using a cut tip is being demonstrated for the first time here (see Video S1).

After deposition, a thermal treatment at 100 °C for 30 min was realized. Figure 5 shows two photographs (back and front), SEM images, and UV-Vis spectra (taken in 4 regions) of the $MAPbI_3$ (Figures 5a-5c) and CsFAMA (Figures 5d-5f) perovskite films deposited by spin-coating with the cut tip. Thus, it was observed that after adaptations in the deposition parameters, it was possible to obtain films without visible defects via spin-coating. However, the amount of perovskite precursor solution necessary to fully cover the 5 cm × 5 cm substrate (600 μL) enhances the cost of this process and leads to high material waste.

The morphology of the spin-coated layers was examined by FEG-SEM images, as shown in Figures 5b and 5e. The top view SEM images indicate that the spin-coating layers from $MAPbI_3$ in DMF:DMSO (4:1) v/v (Figure 5b) and CsFAMA in DMF:DMSO (4:1) v/v (Figure 5e) are compact and free of pinholes. Nevertheless, from the inset images acquired with enhanced magnification, we can see that the grain sizes are not homogenous, thus revealing that these films are still not ideal to achieve the highest efficiency. To characterize the overall uniformity of the perovskite films onto the substrate area, UV-Vis absorption spectra were collected in 4 regions of the $MAPbI_3$ and CsFAMA films, as shown in Figures 5c and 5f, respectively. The films showed average thicknesses of 312 nm ($MAPbI_3$ film) and 504 nm (CsFAMA film). Such thickness values have been considered ideal according to the literature (around 300 nm[53] for $MAPbI_3$, and 400-500 nm[34] for CsFAMA).

Large area perovskite films via blade-coating

The blade-coating method is a scalable technique that has been used to manufacture large-area PSCs, mainly for the deposition of the perovskite layer.[25,28,54] Although this is a scalable technique, deposition of uniform, pinhole-free and homogeneous perovskite layers by this method is also challenging.[55-58] In the blade-coating method, the thickness of the perovskite film can be controlled by the concentration

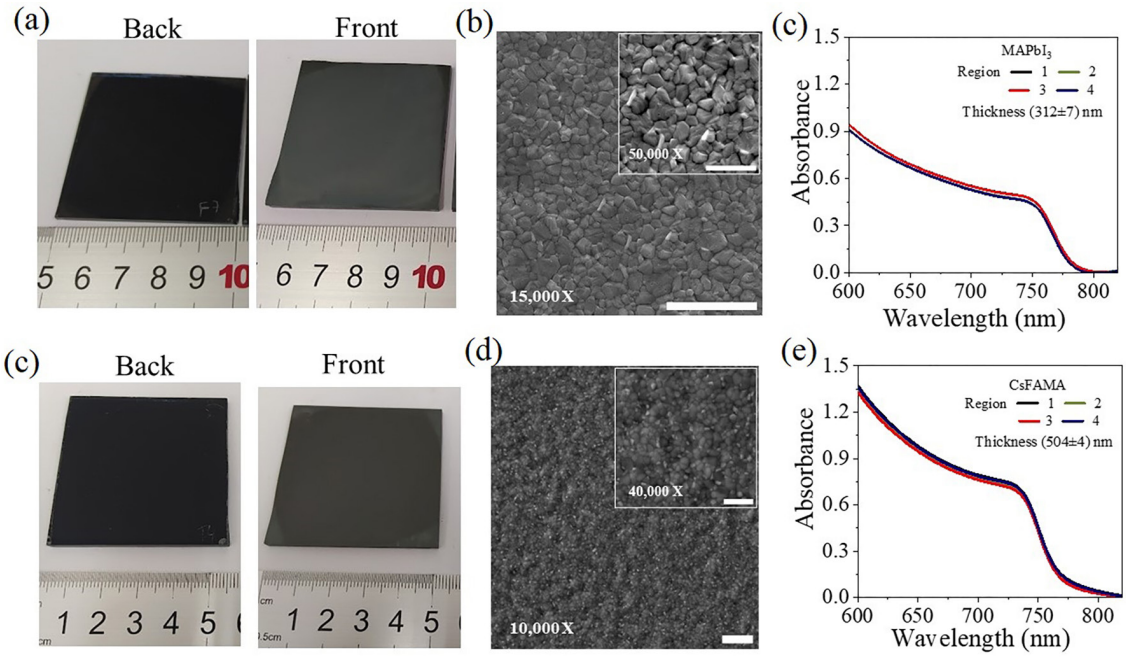

Figure 5. Perovskite films deposited by spin-coating (antisolvent approach) on FTO substrates. Photograph (back and front) of (a) $MAPbI_3$ and (d) CsFAMA films. Morphological characterization of films obtained through top view FEG-SEM images of (b) $MAPbI_3$ and (e) CsFAMA. UV-Vis spectra (collected in four regions) of the perovskite films deposited by spin-coating using a micropipette tip of 1 mL with a cut about 2 cm from its edge: (c) $MAPbI_3$ and (f) CsFAMA perovskites. The scale bar represents 2 μm and 1 μm (insets) in FEG-SEM images.

of the perovskite solution, the gap between the blade and the substrate, and the blade speed.[59] This method requires the application of a process to assist film drying and crystallization, such as the use of high temperature (hot-assisted blade-coating) or the use of air-knife with N_2 or dry air flow (air-knife-assisted blade-coating).[48,56,60-64] Here, we chose to work with the air-knife-assisted blade-coating process for the deposition of perovskite films. The films were deposited inside a glass box containing dry air (Figure S5a, SI section) to maintain an atmosphere of around 20% relative humidity. The air knife system was adapted using a printed part with the aid of a 3D printer (Figure S5b), containing an opening of approximately 2 mm for the air outlet.

$MAPbI_3$ perovskite films were prepared using the precursor solution described in Table 1. The protocol followed for the preparation of perovskite films by blade-coating was based on the work of Marques *et al.*[48] which used a mixture of $PbCl_2$, $Pb(Ac)_2$ and MAI in 2-ME with a 0.5 M concentration for the fabrication of inverted lab-scale PSCs with an active area of 0.045 cm^2. $MAPbI_3$ perovskite films using the same mixture but with DMF as solvent and with 1.0 M concentration were also investigated. Both solvents (2-ME and DMF) have presented good results, however, 2-ME has been more promising for the blade-coating of perovskite films.[48,65-67]

Figure S6 (SI section) shows $MAPbI_3$ films prepared from precursor solutions of 2-ME (Figure S6a) and DMF (Figure S6b), deposited by blade-coating at 50 °C with a blade height of 50 μm, a volume of 30 μL of solutions with different concentrations (0.5 or 1 M) and blade speed of 10 or 15 mm s^{-1}. Figure S6 shows that, for both solvents, there are darker regions at some points of the perovskite film, which suggest that in those regions, the film may be thicker. From these results, we performed further tests by increasing the amount of solution used for the coating. The ideal amount was found to be 80 μL of the perovskite precursor solution, sufficient to homogeneously cover substrates with a size of 5 cm × 5 cm. Video S2 shows the deposition of a perovskite film ($MAPbI_3$ in 2-ME) by blade-coating at 50 °C, with a gap between the blade and substrate of 50 μm and a speed of 10 mm s^{-1}.

From the tests carried out, we chose a concentration of 0.5 M for $MAPbI_3$ in 2-ME, and 1.0 M for $MAPbI_3$ in DMF, using a total amount of solution of 80 μL for deposition of perovskite films. After deposition, a thermal treatment at 100 °C for 30 min was performed to promote solvent removal and assist crystallization. As shown in Figures 6a and 6d, the photographs of these blade-coated perovskite films indicate that the use of both conditions resulted in films with uniform appearance to the bare eye. To investigate the morphology of the films, we performed SEM measurements. Through SEM images displayed in Figures 6b and 6e, it is possible to observe that both the $MAPbI_3$ film in 2-ME and the $MAbI_3$ film in DMF are pinhole-free, but show the presence of small

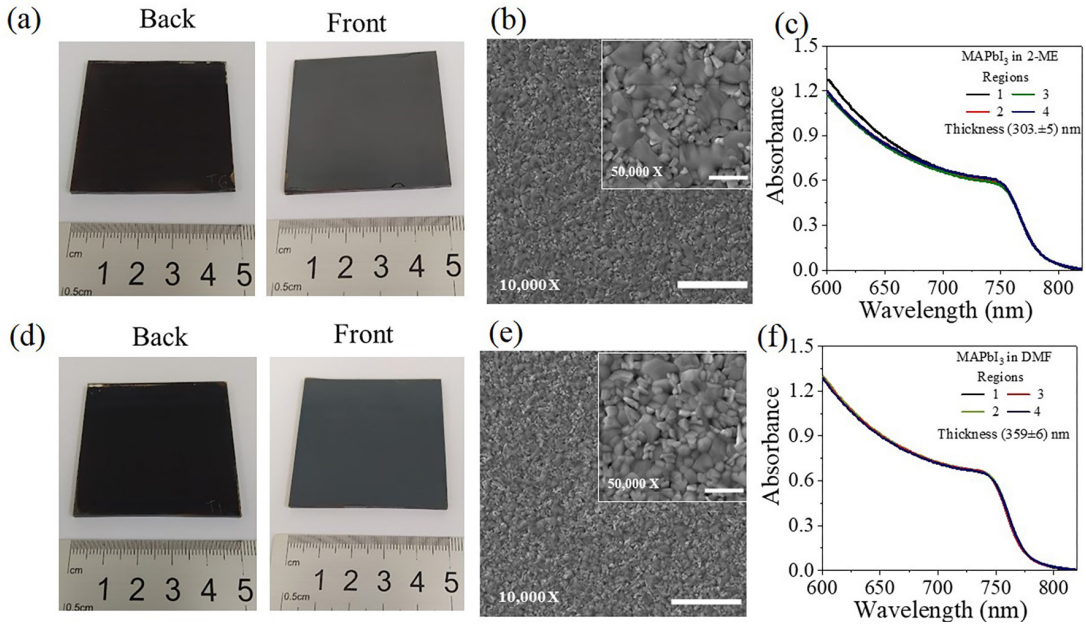

Figure 6. Perovskite films are deposited by blade-coating (air-knife-assisted blade-coating). Photograph (back and front) of perovskite films deposited from solutions of: (a) $MAPbI_3$ in 2-ME (0.5 M) and (d) $MAPbI_3$ in DMF (1.0 M). Morphological characterization of films obtained through top view FEG-SEM images of films deposited from: (b) $MAPbI_3$ in 2-ME (0.5 M) and (e) $MAPbI_3$ in DMF (1.0 M). UV-Vis spectra (collected in 4 regions) and average thickness of the perovskite films deposited by blade-coating: (c) $MAPbI_3$ in 2-ME (0.5 M) and (f) $MAPbI_3$ in DMF (1.0 M). The scale bar represents 2 μm in FEG-SEM images.

grains in some points of the film. This non-uniformity in grain size can be a consequence of a slow drying of the film during coating due to the low temperature of the blade-coating platform (50 °C). The uniformity of the films was also evaluated using measurements of UV-Vis in 4 different regions of each film (Figures 6c and 6e). A more homogeneous response was observed for the film deposited from 2-ME precursor solution. The average thicknesses for the films of $MAPbI_3$ in 2-ME and in DMF were 303 ± 5 and 359 ± 6 nm, respectively. In many works, a thickness around 300 nm is considered ideal for cells containing the $MAPbI_3$ perovskite.[53,68] Thus, our blade-coated films present thicknesses close to the ideal value reported in the literature.

Hole transport layer (HTL)

After deposition of the perovskite layer, a hole transport layer is commonly used in a conventional PSC (Figure 1d). The hole transport material (HTM) most used in PSCs is spiro-OMeTAD. However, due to the high cost, this material has been replaced by other materials, aiming to reduce the cost of manufacturing on an industrial scale.[69-71] In addition, the dopants (tBP, FK209, and LiTFSI) used in combination with spiro-OMeTAD to improve charge transport also possess high costs.[72]

In this work, spiro-OMeTAD solution (with dopants FK209, tBP, and LiTFSI) was deposited using the same conditions developed for the manufacture of lab-scale PSCs. This material was used as a reference. To cover the entire surface of the 5 cm × 5 cm substrate, it was necessary to use 600 μL of the spiro-OMeTAD solution. Figures 7a-7b show the photograph of the bare FTO substrate and spiro-OMeTAD film deposited by spin-coating on the FTO substrate. UV-Vis absorption spectra taken in 4 regions of the spiro-OMeTAD film, with maxima of the main absorption band located at around 375 nm, are shown in Figure 7b. We also observed less intense absorption bands with maxima at about 510 and 470 nm, which indicate the formation of an oxidized spiro-OMeTAD cation radical.[73] The average thickness of the spiro film was 171 ± 3 nm, an optimum value for obtaining high-efficiency PSCs.[34,74,75]

The second HTM investigated in this study was the conjugated polymer P3HT, because of the promising results (high efficiency and improved stability) recently reported using this material[76,77] and also because it is more economically viable than the spiro-OMeTAD.[69] P3HT has high hole mobility, easy processability and good optoelectronic properties.[78]

The P3HT solution without dopants (concentration of 30 mg mL^{-1} in CB) was deposited using two deposition techniques, spin-coating or blade-coating. A volume of 600 μL of this solution was used to cover the entire area of the FTO substrate for films deposited by spin-coating, and a volume of 80 μL of the P3HT solution was used for films deposited by blade-coating. The deposition of the P3HT film by blade-coating is demonstrated in Video S3.

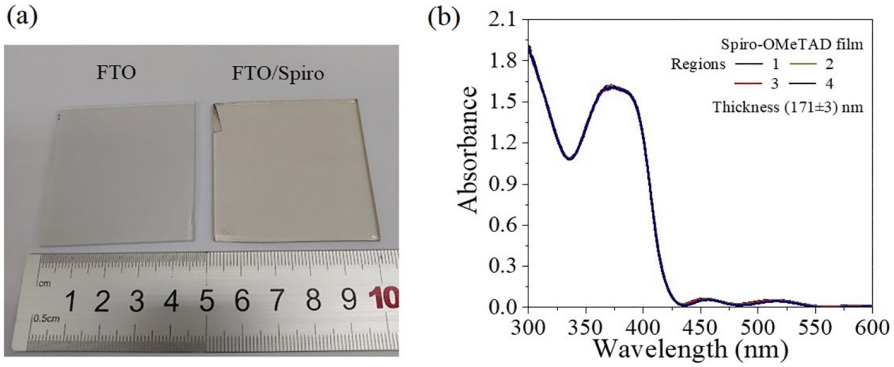

Figure 7. (a) Photos of the bare FTO substrate (left) and spiro-OMeTAD film (right) deposited by spin-coating on the FTO substrate (5 cm × 5 cm). (b) UV-Vis spectra collected in 4 regions of the FTO/spiro-OMeTAD film deposited by spin-coating, with an average thickness of 171 nm.

Figure 8 shows photos and absorption spectra of the P3HT films deposited by spin-coating or blade-coating using different speeds. In both deposition methods, homogeneous P3HT films were obtained over the entire substrate area, as can be seen in photos displayed in Figures 8a-8b. The uniformity can also be verified through the UV-Vis spectra taken in 4 regions of the P3HT/FTO films, as shown in Figure S7 (SI section).

The absorption spectra of P3HT films deposited under different conditions are shown in Figures 8c-8d. For all depositions that resulted in P3HT films with different thicknesses, we can observe an absorbance band with maxima centered at 512 nm (maximum absorption), with shoulders at 550 and 600 nm, which can be attributed to the π-π∗ transition in crystalline π-π stacking structure of P3HT chains.[79] Table 4 presents the parameters used for

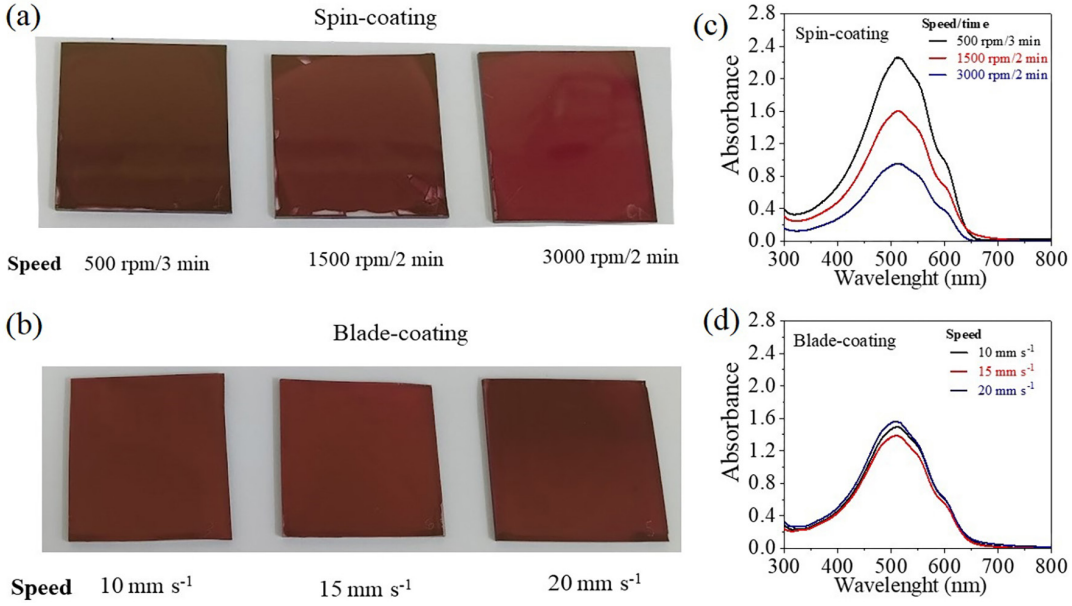

Figure 8. Photos of the P3HT films deposited on FTO substrates (5 cm × 5 cm) at different speeds (a) spin-coating and (b) blade-coating. UV-Vis spectra of the P3HT/FTO films deposited by (c) spin-coating and (d) blade-coating.

Table 4. Deposition parameters and thickness of the P3HT films

Deposition method	Speed/time	Acceleration / (rpm s^{-1})	Thickness / nm
Spin-coating	500 rpm/3 min	500	314 ± 4
	1500 rpm/2 min	1500	222 ± 3
	3000 rpm/2 min	3000	137 ± 2
	Speed / (mm s^{-1})	Gap / μm	
Blade-coating	10	50	197 ± 3
	15		189 ± 4
	20		216 ± 3

the formation of P3HT films and the average thickness measured in 4 different regions of each film. Overall, the thickness values obtained here are close to the optimal values (200-300 nm) reported by Saliba *et al*.[34]

In summary, the deposition techniques used were suitable to obtain thin layers of c-TiO_2, meso-TiO_2, perovskite, spiro-OMeTAD and P3HT in large-area substrates (5 cm × 5 cm). Then, the next step consisted of manufacturing the large-area perovskite solar cells using the main parameters of the deposition defined in the previous steps.

Complete large-area perovskite solar cells and mini-modules

Large-area PSCs were prepared by stacking the layers of different materials with the following n-i-p architecture: glass/FTO/c-TiO_2/meso-TiO_2/Perovskite/P3HT or spiro-OMeTAD/Au (Figure 9a). The devices were assembled using 5 cm × 5 cm FTO substrates as a basis, in which the final active area was delimited to 9 cm^2 by the design of the Au back contact. For the assembly of large-area PSCs, we used the FTO substrate patterned according to the process illustrated in Figure S1 (SI section). For the assembly of a perovskite mini-module, we used the FTO substrate patterned according to the process in Figure S2 (SI section). Table S2 (SI section) shows a summary of the main results with the deposition methods used for each layer and obtained thickness. Optimum layers thickness values used as reference were based on the work of Saliba *et al*.[34] For the Au metallization mask, a piece of Kapton tape was used to delimit the active area (Figure S8, SI section). Figure 9b shows a photograph of the large-area perovskite solar cell (active area = 9 cm^2) assembled on a 5 cm × 5 cm-sized glass-FTO substrate.

J-V curves under illumination (100 mW cm^{-2}) are shown in Figures 9c-9f, with the PCE values obtained from reverse scan displayed as inset. The photovoltaic parameters short-circuit current density (J_{sc}), open-circuit voltage (V_{oc}), fill factor (FF), and PCE extracted from the J-V curves are summarized in Table 5.

$MAPbI_3$ devices in DMF:DMSO deposited by spin-coating (Figure 9c) or $MAPbI_3$ devices in DMF deposited by blade-coating (Figure 9d) achieved a V_{oc} around 1 V and PCEs around 6%. In these devices, spiro-OMeTAD was used as HTL. The low efficiency is related to the low FF value, which is affected by the series resistance (R_s) of the FTO substrate (5 cm × 5 cm). R_s is directly related with the size of the FTO substrate. A better charge extraction in large-area solar cells is usually achieved through the addition of a metallic grid on the FTO substrate. This step is important to minimize the impact of the resistive losses in the FTO substrate and, in this way, improve the photovoltaic parameters of the large-area device. More information on the use of metallic grids in PSCs can be consulted in the literature.[80]

Video S4 shows a fan running with power supplied by the large-area PSC. Furthermore, a PSM was assembled by connecting two large-area PSCs in series, as demonstrated

Table 5. Photovoltaic parameters of the large-area PSCs with an active area of 9 cm^2 measured under illumination (100 mW cm^{-2}). The values in parenthesis are for the best devices from Figure 9. Average and standard deviation values were obtained based on three devices. The device structure is glass/FTO/c-TiO_2/meso-TiO_2+Perovskite/HTL/Au

Perovskite (deposition method)	HTL	Scan	V_{oc} / V	J_{sc} / (mA cm^{-2})	FF / %	PCE / %
$MAPbI_3$ in DMF:DMSO (spin-coating)	Spiro-OMeTAD	R	1.10 ± 0.01 (1.10)	19.21 ± 0.68 (20.17)	28.44 ± 1.08 (26.97)	5.97 ± 0.10 (5.99)
		F	1.08 ± 0.01 (1.07)	19.05 ± 0.75 (20.11)	27.92 ± 0.58 (27.13)	5.74 ± 0.07 (5.84)
$MAPbI_3$ in DMF (blade-coating)	Spiro-OMeTAD	R	1.02 ± 0.02 (1.04)	17.78 ± 0.05 (17.73)	32.71 ± 0.47 (32.24)	5.93 ± 0.2 (5.95)
		F	1.02 ± 0.02 (1.03)	17.59 ± 0.09 (17.50)	31.74 ± 0.15 (31.59)	5.67 ± 0.3 (5.70)
$MAPbI_3$ in 2-ME (blade-coating)	Spiro-OMeTAD	R	0.98 ± 0.02 (0.95)	17.01 ± 1.24 (17.21)	32.35 ± 0.23 (32.11)	5.14 ± 0.12 (5.25)
		F	0.97 ± 0.03 (0.94)	16.67 ± 1.13 (16.91)	32.35 ± 0.23 (32.32)	5.14 ± 0.12 (5.14)
CsFAMA in DMF:DMSO (spin-coating)	Spiro OMeTAD	R	0.99 ± 0.02 (1.01)	15.07 ± 0.79 (16.13)	30.87 ± 1.15 (29.2)	4.59 ± 0.19 (4.77)
		F	0.97 ± 0.02 (0.99)	15.09 ± 0.82 (16.15)	29.82 ± 0.89 (28.79)	4.35 ± 0.18 (4.60)
CsFAMA in DMF:DMSO (spin-coating)	P3HT	R	0.68 ± 0.01 (0.69)	9.09 ± 0.05 (9.14)	26.02 ± 0.44 (25.58)	1.60 ± 0.02 (1.61)
		F	0.66 ± 0.03 (0.68)	9.07 ± 0.03 (9.1)	25.25 ± 1.08 (24.17)	1.49 ± 0.01 (1.50)

MA: methylammonium; FA: formamidinium; Cs: cesium; $MAPbI_3$: methylammonium lead iodide; Spiro-OMeTAD: 2,2',7,7'tetrakis-(*N*,*N*-di-4-methoxyphenylamino)-9,9'-spirobi-fluorenes; P3HT: poly(3-hexylthiophene); DMF: dimethyl formamide; DMSO: dimethyl sulfoxide; 2-ME: 2-methoxyethanol; R: reverse scan; F: forward scan; J_{sc}: short-circuit current density; V_{oc}: open-circuit voltage; FF: fill factor; PCE: power conversion efficiency.

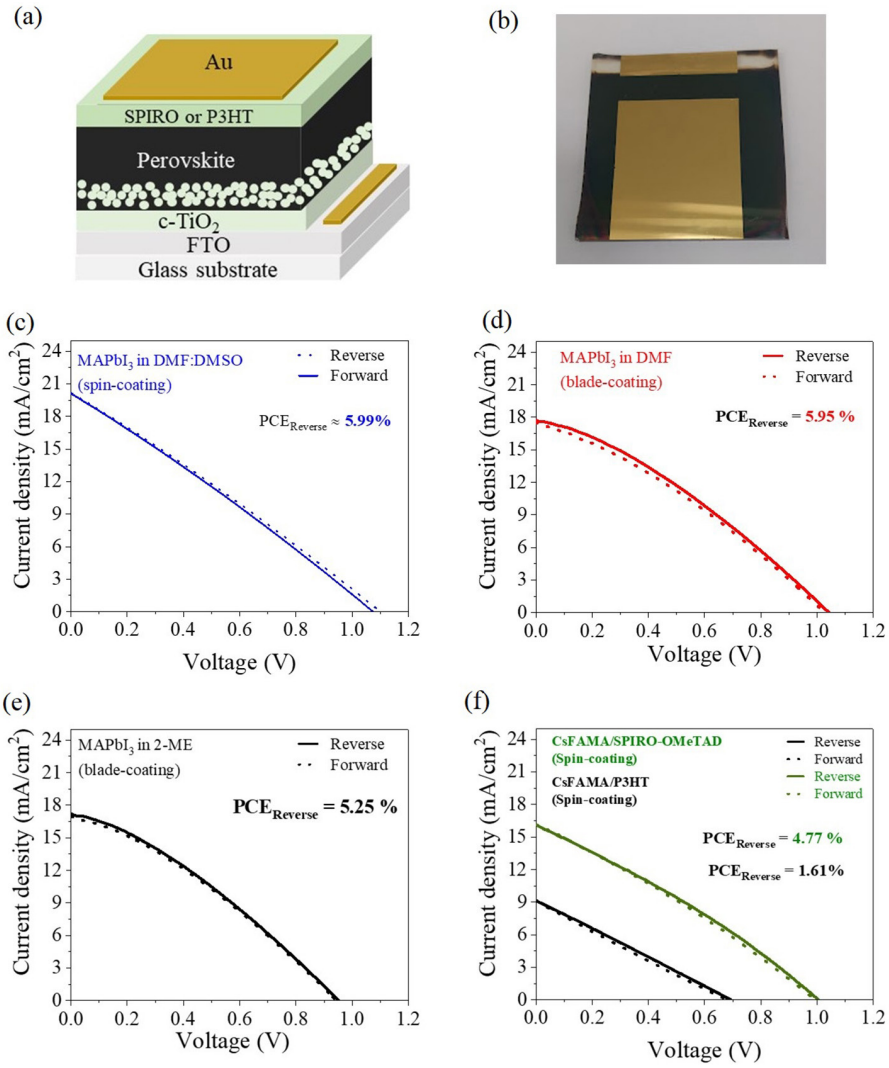

Figure 9. (a) Schematic diagram of the mesoporous n-i-p large-area PSC. (b) Photograph of a complete large-area perovskite solar cell. (c-f) J-V curves (reverse and forward scans) of best devices prepared with different perovskite/HTL compositions, with an active area of 9 cm^2 under illumination (100 mW cm^{-2}, AM 1.5 G simulated irradiation).

in Figure 10a. Under illumination, this PSM achieved a V_{oc} of approximately 1.9 V (Figure 10b). This voltage was enough to turn on a red or a yellow commercial LED (Figure 10c). Video S5 shows the red LED being lit.

Then, a monolithic mini-PSM containing two series-connected solar cells (active area of 4.5 cm^2 each) in the same FTO substrate (5 cm × 5 cm total substrate area) was fabricated. For that, we used a 5 cm × 5 cm FTO substrate patterned according to the method described in "Substrate preparation sub-section" (Figure S2), and the layers were deposited according to the parameters described in Table S2, resulting in a device with a structure of glass/FTO/c-TiO_2/meso-TiO_2+$MAPbI_3$ in DMF by blade-coating/spiro-OMeTAD/Au. The active area of the PSM was delimited using Kapton tape (Figure S9). Figure 11 shows photographs of the monolithic mini-PSM, back and front, and the J-V curve under illumination (100 mW cm^{-2}). This

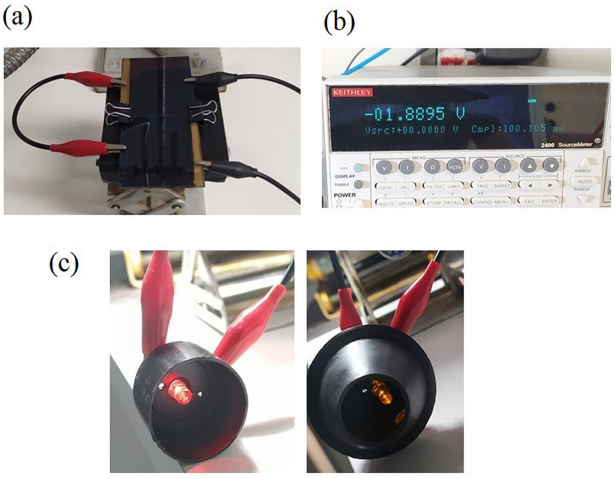

Figure 10. (a) Perovskite solar module obtained by connecting in series two large-area PSCs with an active area of 9 cm^2 each. (b) The voltage generated by the PSM. (c) Red LED and yellow LED are turned on by this PSM.

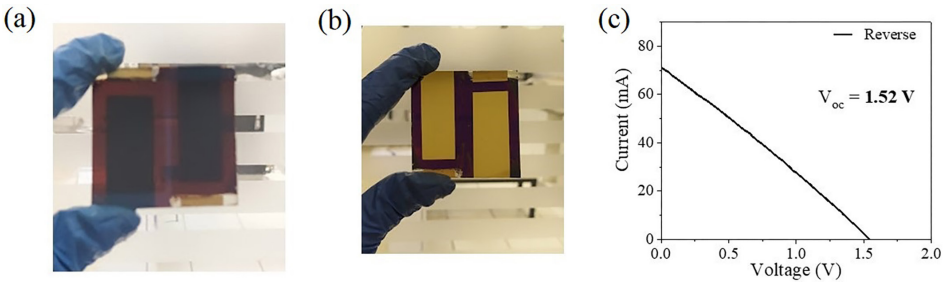

Figure 11. Photographs of the monolithic mini-PSM: (a) back and (b) front views. (b) J-V curve of the monolithic mini-PSM under illumination (100 mW cm^{-2}).

mini-PSM achieved a V_{oc} around 1.5 V. This voltage was also used to turn on a red LED (see Video S6).

Usually, the manufacturing of monolithic perovskite mini-modules is complicated because it requires sophisticated techniques, including the use of lasers (for the scribing process, i.e., delimiting the area of the layers and interconnection spaces) and/or lithography processes for patterning the substrates. Here, we demonstrated a facile method for the assembly of a series-connected monolithic mini-module, and a large-area single cell, using FTO substrates of 5 cm × 5 cm as a starting point, in a chemistry lab, without the use of those techniques. We discuss the need to adapt previously developed recipes for small PSCs (ca. 0.1 cm^2 active area) to get functional large-area cells and mini-modules, demonstrating key points in the solution-processing of each device layer. The best perovskite films achieved here presented full substrate coverage, without pinholes, with a sufficiently uniform absorption characteristics throughout the active area. However, from SEM images, it was observed that grain size still showed some inhomogeneities, leaving room to further improvements in those films. Regardless of that fact and the low FF values, which limited the maximum PCE to 6%, this is the first report of a large-area perovskite cell and perovskite mini-module assembled in Brazil, using only available machinery and facile procedures in a Chemistry lab, which opens up the opportunity for new groups starting in the area.

Conclusions

In summary, this work provides a preparation protocol for the manufacture of large-area PSCs and mini-modules containing two series-connected cells using facile methods, without complex techniques or processes, and materials that could be easily found in a Chemistry research laboratory. The large-area devices (active area of 9 cm^2) manufactured achieved an open-circuit voltage of around 1.1 V. A prototype with two large-area cells connected in series provided an open-circuit voltage of approximately 1.9 V. A monolithic PSM (manufactured without the use of lasers or lithography) was also assembled and achieved a voltage of 1.52 V. Both modules were able to turn on a red LED. This is the first scientific report demonstrating a large-area single n-i-p perovskite cell and mini-module assembled in Brazil.

Supplementary Information

Supplementary information and videos S1 to S6 are available free of charge at http://jbcs.sbq.org.br.

Acknowledgments

All authors gratefully acknowledge support from the São Paulo Research Foundation, FAPESP, (grants 17/11986-5) and Shell. F.L.A. acknowledges FAPESP (20/14451-8). We also thank Rodrigo Szostak for contributing to the assembly of the air-knife system for the blade-coating equipment and for developing the J-V curves measurement software, and José M. C. Silva Filho for assisting with SEM measurements.

Author Contributions

F. L. A. optimized the method for the preparation of perovskite films and large area PSCs and created the method for assembling perovskite solar modules, assembled and characterized the devices, analyzed data and wrote the original draft. F. L. A., J. N. F., and A. F. N. conceived the idea and conceptualize the work. J. N. F. and A. F. N. carried out review and editing of the manuscript, supervised the project and got the funding.

References

1. Snaith, H. J.; *J. Phys. Chem. Lett.* **2013**, *4*, 3623. [Crossref]
2. Green, M. A.; Ho-Baillie, A.; Snaith, H. J.; *Nat. Photonics* **2014**, *8*, 506. [Crossref]
3. Breternitz, J.; Schorr, S.; *Adv. Energy Mater.* **2018**, *8*, 1802366. [Crossref]
4. Li, D.; Shi, J.; Xu, Y.; Luo, Y.; Wu, H.; Meng, Q.; *Natl. Sci. Rev.* **2018**, *5*, 559. [Crossref]
5. de Mayrinck, C.; da Fonseca, A. F. V.; Schiavon, M. A.; *Quim. Nova* **2020**, *43*, 1264. [Crossref]

6. Moral, R. F.; Hermsdorff, A. B.; Marchezi, P. E.; Germino, J. C.; Bonato, L. G.; de Araújo, F. L.; Nogueira, A. F.; *J. Braz. Chem. Soc.* **2022**, *33*, 997. [Crossref]
7. Raphael, E.; Silva, M. N.; Szostak, R.; Schiavon, M. A.; Nogueira, A. F.; *Quim. Nova* **2018**, *41*, 61. [Crossref]
8. Seok, S. Il; Guo, T.-F.; *MRS Bull.* **2020**, *45*, 427. [Crossref]
9. Huang, J.; Yuan, Y.; Shao, Y.; Yan, Y.; *Nat. Rev. Mater.* **2017**, *2*, 17042. [Crossref]
10. Miyata, A.; Mitioglu, A.; Plochocka, P.; Portugall, O.; Wang, J. T.-W.; Stranks, S. D.; Snaith, H. J.; Nicholas, R. J.; *Nat. Phys.* **2015**, *11*, 582. [Crossref]
11. Stranks, S. D.; Eperon, G. E.; Grancini, G.; Menelaou, C.; Alcocer, M. J. P.; Leijtens, T.; Herz, L. M.; Petrozza, A.; Snaith, H. J.; *Science* **2013**, *342*, 341. [Crossref]
12. Herz, L. M.; *ACS Energy Lett*. **2017**, *2*, 1539. [Crossref]
13. Manser, J. S.; Christians, J. A.; Kamat, P. V.; *Chem. Rev.* **2016**, *116*, 12956. [Crossref]
14. Song, Z.; McElvany, C. L.; Phillips, A. B.; Celik, I.; Krantz, P. W.; Watthage, S. C.; Liyanage, G. K.; Apul, D.; Heben, M. J.; *Energy Environ. Sci.* **2017**, *10*, 1297. [Crossref]
15. Rong, Y.; Hou, X.; Hu, Y.; Mei, A.; Liu, L.; Wang, P.; Han, H.; *Nat. Commun.* **2017**, *8*, 14555. [Crossref]
16. Best Research-Cell Efficiencies Chart, https://www.nrel.gov/pv/assets/pdfs/best-research-cell-efficiencies-rev220630.pdf, accessed in November 2022.
17. Green, M. A.; Dunlop, E. D.; Hohl-Ebinger, J.; Yoshita, M.; Kopidakis, N.; Hao, X.; *Prog. Photovoltaics Res. Appl.* **2022**, *30*, 3. [Crossref]
18. Chen, S.; Xiao, X.; Gu, H.; Huang, J.; *Sci. Adv.* **2021**, *7*. [Crossref]
19. NREL-Champion Module Efficiencies, https://www.nrel.gov/pv/assets/pdfs/champion-module-efficiencies-rev220202.pdf, accessed in November 2022.
20. Wang, Y.; Duan, C.; Lv, P.; Ku, Z.; Lu, J.; Huang, F.; Cheng, Y.-B.; *Natl. Sci. Rev.* **2021**, *8*, nwab075. [Crossref]
21. Yan, J.; Savenije, T. J.; Mazzarella, L.; Isabella, O.; *Sustainable Energy Fuels* **2022**, *6*, 243. [Crossref]
22. Rong, Y.; Hu, Y.; Mei, A.; Tan, H.; Saidaminov, M. I.; Seok, S. Il; McGehee, M. D.; Sargent, E. H.; Han, H.; *Science* **2018**, *361*. [Crossref]
23. Saki, Z.; Byranvand, M. M.; Taghavinia, N.; Kedia, M.; Saliba, M.; *Energy Environ. Sci.* **2021**, *14*, 5690. [Crossref]
24. Soto-Montero, T.; Soltanpoor, W.; Morales-Masis, M.; *APL Mater.* **2020**, *8*, 110903. [Crossref]
25. Hamukwaya, S. L.; Hao, H.; Zhao, Z.; Dong, J.; Zhong, T.; Xing, J.; Hao, L.; Mashingaidze, M. M. A.; *Coatings* **2022**, *12*, 252. [Crossref]
26. Li, D.; Zhang, D.; Lim, K.-S.; Hu, Y.; Rong, Y.; Mei, A.; Park, N.-G.; Han, H.; *Adv. Funct. Mater.* **2021**, *31*, 2008621. [Crossref]
27. Hu, Y.; Si, S.; Mei, A.; Rong, Y.; Liu, H.; Li, X.; Han, H.; *Sol. RRL* **2017**, *1*, 1600019. [Crossref]
28. Matteocci, F.; Vesce, L.; Kosasih, F. U.; Castriotta, L. A.; Cacovich, S.; Palma, A. L.; Divitini, G.; Ducati, C.; Di Carlo, A.; *ACS Appl. Mater. Interfaces* **2019**, *11*, 25195. [Crossref]
29. Agresti, A.; Pescetelli, S.; Palma, A. L.; Martín-García, B.; Najafi, L.; Bellani, S.; Moreels, I.; Prato, M.; Bonaccorso, F.; Di Carlo, A.; *ACS Energy Lett.* **2019**, 1862. [Crossref]
30. Matteocci, F.; Castriotta, L. A.; Palma, A. L. In *Photoenergy and Thin Film Materials*; John Wiley & Sons, Inc.: Hoboken, NJ, USA, 2019, ch. 3, p. 121-155.
31. Palma, A. L.; Matteocci, F.; Agresti, A.; Pescetelli, S.; Calabrò, E.; Vesce, L.; Christiansen, S.; Schmidt, M.; Di Carlo, A.; *IEEE J. Photovoltaics* **2017**, *7*, 1674. [Crossref]
32. Castriotta, L. A.; Zendehdel, M.; Yaghoobi Nia, N.; Leonardi, E.; Löffler, M.; Paci, B.; Generosi, A.; Rellinghaus, B.; Di Carlo, A.; *Adv. Energy Mater.* **2022**, *12*, 2103420. [Crossref]
33. Yang, M.; Kim, D. H.; Klein, T. R.; Li, Z.; Reese, M. O.; Tremolet de Villers, B. J.; Berry, J. J.; van Hest, M. F. A. M.; Zhu, K.; *ACS Energy Lett.* **2018**, *3*, 322. [Crossref]
34. Saliba, M.; Correa-Baena, J.-P.; Wolff, C. M.; Stolterfoht, M.; Phung, N.; Albrecht, S.; Neher, D.; Abate, A.; *Chem. Mater.* **2018**, *30*, 4193. [Crossref]
35. Prathapani, S.; More, V.; Bohm, S.; Bhargava, P.; Yella, A.; Mallick, S.; *Appl. Mater. Today* **2017**, *7*, 112. [Crossref]
36. Möllmann, A.; Gedamu, D.; Vivo, P.; Frohnhoven, R.; Stadler, D.; Fischer, T.; Ka, I.; Steinhorst, M.; Nechache, R.; Rosei, F.; Cloutier, S. G.; Kirchartz, T.; Mathur, S.; *Adv. Eng. Mater.* **2019**, *21*, 1801196. [Crossref]
37. Wang, Y.; Yang, L.; Dall'Agnese, C.; Chen, G.; Li, A. J.; Wang, X. F.; *Front. Chem. Sci. Eng.* **2020**, *15*, 180. [Crossref]
38. Kavan, L.; Tétreault, N.; Moehl, T.; Grätzel, M.; *J. Phys. Chem. C* **2014**, *118*, 16408. [Crossref]
39. Wu, R.; Yang, B.; Xiong, J.; Cao, C.; Huang, Y.; Wu, F.; Sun, J.; Zhou, C.; Huang, H.; Yang, J.; *J. Renewable Sustainable Energy* **2015**, *7*, 043105. [Crossref]
40. Zhang, H.; Wang, H.; Ma, M.; Wu, Y.; Dong, S.; Xu, Q.; *Sol. RRL* **2018**, *2*, 1800097. [Crossref]
41. Parida, B.; Singh, A.; Oh, M.; Jeon, M.; Kang, J.-W.; Kim, H.; *Mater. Today Commun.* **2019**, *18*, 176. [Crossref]
42. da Silva, J. C.; de Araújo, F. L.; Szostak, R.; Marchezi, P. E.; Moral, R. F.; de Freitas, J. N.; Nogueira, A. F.; *J. Mater. Chem. C* **2020**, *8*, 9697. [Crossref]
43. Ahn, S. H.; Jeon, H.; Son, K. J.; Ahn, H.; Koh, W.-G.; Ryu, D. Y.; Kim, J. H.; *J. Mater. Chem.* **2011**, *21*, 1772. [Crossref]
44. Tailor, N. K.; Abdi-Jalebi, M.; Gupta, V.; Hu, H.; Dar, M. I.; Li, G.; Satapathi, S.; *J. Mater. Chem. A* **2020**, *8*, 21356. [Crossref]
45. Germino, J. C.; Szostak, R.; Motti, S. G.; Moral, R. F.; Marchezi, P. E.; Seleghini, H. S.; Bonato, L. G.; de Araújo, F. L.; Atvars, T. D. Z.; Herz, L. M.; Fenning, D.; Hagfeldt, A.; Nogueira, A. F.; *ACS Photonics* **2020**, *7*, 2282. [Crossref]

46. Marchezi, P. E.; de Araújo, F. L.; Szostack, R.; Germino, J. C.; Therézio, E. M.; Marletta, A.; Nogueira, A. F.; *J. Mater. Chem. C* **2021**, *9*, 14648. [Crossref]
47. Scalon, L.; Szostak, R.; Araújo, F. L.; Adriani, K. F.; Silveira, J. F. R. V.; Oliveira, W. X. C.; da Silva, J. L. F.; Oliveira, C. C.; Nogueira, A. F.; *J. Am. Chem. Soc.* **2022**, *6*, 1306. [Crossref]
48. Marques, A. S.; Faria, R. M.; Freitas, J. N.; Nogueira, A. F.; *Ind. Eng. Chem. Res.* **2021**, *60*, 7145. [Crossref]
49. Wang, C.; Tan, G.; Luo, X.; Li, J.; Gao, X.; Mo, Y.; Zhang, X.-L.; Wang, X.; Huang, F.; *J. Power Sources* **2020**, *466*, 228321. [Crossref]
50. Ren, A.; Lai, H.; Hao, X.; Tang, Z.; Xu, H.; Yu Jeco, B. M. F.; Watanabe, K.; Wu, L.; Zhang, J.; Sugiyama, M.; Wu, J.; Zhao, D.; *Joule* **2020**, *4*, 1263. [Crossref]
51. Agresti, A.; Pescetelli, S.; Palma, A. L.; Del Rio Castillo, A. E.; Konios, D.; Kakavelakis, G.; Razza, S.; Cinà, L.; Kymakis, E.; Bonaccorso, F.; Di Carlo, A.; *ACS Energy Lett.* **2017**, *2*, 279. [Crossref]
52. Tong, G.; Son, D.-Y.; Ono, L. K.; Liu, Y.; Hu, Y.; Zhang, H.; Jamshaid, A.; Qiu, L.; Liu, Z.; Qi, Y.; Tong, G.; Son, D.; Ono, L. K.; Liu, Y.; Hu, Y.; Zhang, H.; Jamshaid, A.; Qiu, L.; Liu, Z.; Qi, Y. B.; *Adv. Energy Mater.* **2021**, *11*, 2003712. [Crossref]
53. Momblona, C.; Malinkiewicz, O.; Roldán-Carmona, C.; Soriano, A.; Gil-Escrig, L.; Bandiello, E.; Scheepers, M.; Edri, E.; Bolink, H. J.; *APL Mater.* **2014**, *2*, 81504. [Crossref]
54. Razza, S.; Castro-Hermosa, S.; Di Carlo, A.; Brown, T. M.; *APL Mater.* **2016**, *4*, 091508. [Crossref]
55. Li, C.; Yin, J.; Chen, R.; Lv, X.; Feng, X.; Wu, Y.; Cao, J.; *J. Am. Chem. Soc.* **2019**, *141*, 6345. [Crossref]
56. Zhong, J.-X.; Wu, W. Q.; Ding, L.; Kuang, D.-B.; *Energy Environ. Mater.* **2021**, *4*, 277. [Crossref]
57. Razza, S.; Di Giacomo, F.; Matteocci, F.; Cinà, L.; Palma, A. L.; Casaluci, S.; Cameron, P.; D'Epifanio, A.; Licoccia, S.; Reale, A.; Brown, T. M.; Di Carlo, A.; *J. Power Sources* **2015**, *277*, 286. [Crossref]
58. Qiu, L.; He, S.; Ono, L. K.; Liu, S.; Qi, Y.; *ACS Energy Lett.* **2019**, *4*, 2147. [Crossref]
59. Yao, H.; Shi, S.; Li, Z.; Ci, Z.; Zhu, G.; Ding, L.; Jin, Z.; *J. Energy Chem.* **2021**, *57*, 567. [Crossref]
60. Wu, W.-Q.; Yang, Z.; Rudd, P. N.; Shao, Y.; Dai, X.; Wei, H.; Zhao, J.; Fang, Y.; Wang, Q.; Liu, Y.; Deng, Y.; Xiao, X.; Feng, Y.; Huang, J.; *Sci. Adv.* **2019**, *5*, eaav8925. [Crossref]
61. Zhang, J.; Bu, T.; Li, J.; Li, H.; Mo, Y.; Wu, Z.; Liu, Y.; Zhang, X. L.; Cheng, Y. B.; Huang, F.; *J. Mater. Chem. A* **2020**, *8*, 8447. [Crossref]
62. Deng, Y.; Zheng, X.; Bai, Y.; Wang, Q.; Zhao, J.; Huang, J.; *Nat. Energy* **2018**, *3*, 560. [Crossref]
63. Lee, D.-K.; Jeong, D. N.; Ahn, T. K.; Park, N.-G.; *ACS Energy Lett.* **2019**, *4*, 2393. [Crossref]
64. Ding, J.; Han, Q.; Ge, Q.-Q.; Liu, J.; Mitzi, D. B.; Hu, J.-S.; Xue, D.-J.; Ma, J.-Y.; Zhao, B.-Y.; Chen, Y.-X.; *Joule* **2019**, *3*, 402. [Crossref]
65. Hendriks, K. H.; Van Franeker, J. J.; Bruijnaers, B. J.; Anta, J. A.; Wienk, M. M.; Janssen, R. A. J.; *J. Mater. Chem. A* **2017**, *5*, 2346. [Crossref]
66. Zhong, Y.; Munir, R.; Li, J.; Tang, M.-C.; Niazi, M. R.; Smilgies, D.-M.; Zhao, K.; Amassian, A.; *ACS Energy Lett.* **2018**, *3*, 1078. [Crossref]
67. Castro-Hermosa, S.; Wouk, L.; Bicalho, I. S.; de Queiroz Corrêa, L.; de Jong, B.; Cinà, L.; Brown, T. M.; Bagnis, D.; *Nano. Res.* **2020**, *14*, 1034. [Crossref]
68. Liu, Y.; Jin, B.; Zhang, H.; Zhang, Y.; Kim, Y.; Wang, C.; Wen, S.; Xu, B.; Im, C.; Tian, W.; *ACS Appl. Mater. Interfaces* **2019**, *11*, 14810. [Crossref]
69. Pham, H. D.; Wu, Z.; Ono, L. K.; Manzhos, S.; Feron, K.; Motta, N.; Qi, Y.; Sonar, P.; *Adv. Electron. Mater.* **2017**, *3*, 1700139. [Crossref]
70. Zhou, P.; Bu, T.; Shi, S.; Li, L.; Zhang, Y.; Ku, Z.; Peng, Y.; Zhong, J.; Cheng, Y.-B.; Huang, F.; *J. Mater. Chem. C* **2018**, *6*, 5733. [Crossref]
71. Hajikhanmirzaei, L.; Shahroosvand, H.; Pashaei, B.; Monache, G. D.; Nazeeruddin, M. K.; Pilkington, M.; *J. Mater. Chem. C* **2020**, *8*, 6221. [Crossref]
72. Onozawa-Komatsuzaki, N.; Funaki, T.; Murakami, T. N.; Kazaoui, S.; Chikamatsu, M.; Sayama, K.; *J. Electrochem. Soc. Jpn.* **2017**, *85*, 226. [Crossref]
73. Hong Noh, J.; Joong Jeon, N.; Chan Choi, Y.; Nazeeruddin, M. K.; Grätzel, M.; *J. Mater. Chem. A* **2013**, *1*, 11842. [Crossref]
74. Kim, G.-W.; Shinde, D. V.; Park, T.; *RSC Adv.* **2015**, *5*, 99356. [Crossref]
75. Marinova, N.; Tress, W.; Humphry-Baker, R.; Dar, M. I.; Bojinov, V.; Zakeeruddin, S. M.; Nazeeruddin, M. K.; Grätzel, M.; *ACS Nano* **2015**, *9*, 4200. [Crossref]
76. Jung, E. H.; Jeon, N. J.; Park, E. Y.; Moon, C. S.; Shin, T. J.; Yang, T.-Y.; Noh, J. H.; Seo, J.; *Nature* **2019**, *567*, 511. [Crossref]
77. Yaghoobi Nia, N.; Lamanna, E.; Zendehdel, M.; Palma, A. L.; Zurlo, F.; Castriotta, L. A.; Di Carlo, A.; *Small* **2019**, *15*, 1904399. [Crossref]
78. Ulfa, M.; Zhu, T.; Goubard, F.; Pauporté, T.; *J. Mater. Chem. A* **2018**, *6*, 13350. [Crossref]
79. Landgrave-Barbosa, F.; Marmolejo-Valencia, A. F.; Baray-Calderón, A.; Hu, H.; Aguilar-Cordero, J. C.; Amador-Bedolla, C.; Ugalde-Saldivar, V. M.; *J. Solid State Electrochem.* **2022**, *26*, 649. [Crossref]
80. da Silva Filho, J. M. C.; Gonçalves, A. D.; Marques, F. C.; de Freitas, J. N.; *Sol. RRL* **2022**, *6*, 2100865. [Crossref]

Submitted: August 24, 2022
Published online: November 29, 2022